Plasma Enhanced Atomic Layer Deposition of Titanium Molybdenum Nitride: Influence of RF Bias and Substrate Structure

Md. Istiaque Chowdhury[1], Mark Sowa[2], Kylie E. Van Meter[3], Tomas F. Babuska[3,4], Tomas Grejtak[3,4], Alexander C. Kozen[5], Brandon A. Krick[3,4], Nicholas C. Strandwitz[1]

[1]Department of Materials Science and Engineering, Lehigh University, Bethlehem PA 18015
[2]Veeco ALD, Waltham, MA 02453
[3]Mechanical Engineering, Florida State University, Tallahassee, FL 32310
[4]Department of Mechanical Engineering and Mechanics, Lehigh University, Bethlehem PA 18015
[5]Department of Materials Science & Engineering, University of Maryland, College Park, MD 20740

In this work, TiMoN thin films were deposited by plasma enhanced atomic layer deposition (PEALD) with an equal number of Ti and Mo precursor exposures at a substrate temperature of 250 °C. Tetrakis(dimethylamido) titanium and bis(tert-butylimido)bis(dimethylamido) molybdenum were used as sources for Ti and Mo respectively. N_2 and N_2/H_2 plasma were used respectively for TiN and MoN cycles as a source for N. Negative RF substrate bias voltage of magnitude, $|V_{bias}|$, 0, 31, 62, 125, and 188 V were applied during the plasma half cycle. Nanocrystalline rock salt crystal structures were found by X-ray diffraction for films deposited on single crystal Si and Si-thermal oxide substrates. Applying $|V_{bias}|$ generated voids by bombardment of high energy ions, lowering the density. Further increase of $|V_{bias}|$ caused annihilation of voids and slight increase in density. Four point probe measurement showed increased electrical resistivity due to reduction in grain size caused by continuous renucleation during growth. High energy ions at high $|V_{bias}|$ sputtered away the films resulting in low growth rates. Stripe test revealed inferior wear rates and coefficients of friction at higher $|V_{bias}|$ due to low density porous

films. Epitaxial films deposited on c-plane sapphire had (111) orientation and considerable mosaicity with twinned domains rotated at 60° to each other.

I. Introduction

Transition metal nitrides, often those based on TiN, have applications as wear resistant coatings for cutting tools,[1] electrode materials,[2,3] and biomedical implants.[4] One of the challenges for this class of materials is to make them even more resistant to high temperature oxidation and abrasive wear.[5] Ternary solid solutions of TiN have been studied to improve the tribological properties of TiN.[6,7] For example, apart from solid solution strengthening in Ti_xAl_yN ternary system,[8] addition of Al to TiN improves oxidation resistance by forming aluminum oxide on the coating surface to prevent oxygen penetration into the film.[9] Further, Ti_xMo_yN[7,10,11] and Ti_xV_yN [12,13] have been reported to reduce the coefficient of friction by forming lubricious oxides of Mo and V, respectively, during dry sliding conditions.

Other than lowering the friction coefficient, addition of Mo to TiN substantially improves mechanical and tribological properties, such as increasing microhardness[7,14], reducing grain size[14], and reducing wear rates.[7,14] Generally, Ti_xMo_yN solid solutions are reported to have a rock salt cubic B1 crystal structure.[7,10,11,15] Although the solid solubility of Mo in α-TiN is reportedly very low under equilibrium condition,[16] a number of solid solutions of Ti_xMo_yN films have been reported, grown mostly by physical vapor deposition.[7,10,11,14,17] We previously reported the growth of $Ti_xMo_{1-x}N$ by plasma enhanced atomic layer deposition (PEALD).[15]

Beyond composition, several tunable parameters are available for modifying PEALD growth conditions that may also effect physical properties including gas composition, gas pressure,

substrate temperature, and RF substrate bias.[18–21] This work is focused on the application of applied RF substrate bias. In vacuum-based plasma systems, the plasma bulk is quasi-neutral with equal densities of negative (mostly) electrons and positive ions. Due to the much higher mobility of electrons, surfaces in contact with the plasma will develop a negative charge relative to the plasma bulk. A thin plasma sheath establishes a potential gradient between the plasma bulk and the surface such that positive and negative charge surface losses are equilibrated. Electrons are repelled from surfaces while positive ions are accelerated into them. Under typical remote plasma conditions, plasma ions will strike an electrically floating or grounded substrate with a distribution of energies up to approximately the plasma potential (~10-50 V for inductively coupled plasmas, depending on plasma conditions including RF power, pressure, gas composition). Applying RF power to the substrate holder when it is in contact with a plasma (substrate bias) increases the average energy of the positive plasma ions striking the substrate surface. This additional ion bombardment energy is an effective way to tune the structure and properties of the deposited film.

Application of RF bias during the plasma half cycle has been shown to impact crystallinity, density, refractive index, stress, resistivity, impurities, stoichiometry, and wet etch rate.[19] AlN deposited by PEALD with N_2-H_2 plasma showed decreased surface roughness, improved crystallinity, higher growth per cycle (GPC), more Al – N bonds, and improvements in electrical properties like higher relative permittivity and drastic reduction of leakage current, within a narrow window of bias magnitude (-35 to -70 V).[20] HfN_x grown by PEALD with H_2 plasma ($CpHf(NMe_2)_3$ precursor acted as the source for both Hf and N) had minimum optical and electrical resistivity and a reduction in oxygen impurity at -130 V substrate bias.[22] At high bias these films were porous and had columnar growth. Thin films of PEALD grown TiN_x and HfN_x using Ar + H_2 and H_2 plasmas respectively (N in TiN_x and HfN_x were supplied from $Ti(NMe_2)_4$ and $CpHf(NMe_2)_3$

precursors respectively), exhibited desirable film properties such as minimum electrical resistivity, maximum density and maximum residual stress at RF substrate bias of –130 V.[18] Density increased for TiN_x and HfN_x films with increasingly negative substrate bias and the residual stress transitioned from tensile to compressive. The oxygen impurity content was also reduced by introduction of negative bias, which led to lower electrical resistivities. PEALD of HfN_x using both H_2 and Ar–H_2 also showed similar response to negative substrate bias.[23] The lowest electrical resistivity, maximum Hf^{3+} concentration in the cation mixture (Hf^{3+} and Hf^{4+}), and lowest impurity content were found at -130 V for H_2 plasma but at -225 V for Ar–H_2 plasma. Therefore, the plasma ion species also plays a large role in determining the outcome of substrate biasing in addition to the magnitude of the bias voltage.

Negative substrate biasing has also been employed during physical vapor deposition, which results in increased hardness,[6,8] a finer columnar grain microstructure,[8,24–26] and a higher adatom mobility due to increased ion energy. The increased mobility causes the valleys of the columnar grains to fill in and results in a smoother film surface.[8,24] Furthermore, the high energy bombardment of ionized species on the reaction surface causes high compressive stress by embedding ions in the film[8,26,27] and also densification by elimination of voids through faster adatom mobility.[28,29] Ljungcrantz et al. demonstrated that the defect concentration is higher at low bias magnitudes resulting in higher compressive residual stress compared to films grown at higher bias magnitudes where the compressive stress decreases by annihilation of defects due to higher adatom mobility.[25] In other cases, it has been shown that the defect concentration in the films increases with bias voltages.[6,8] In terms of crystallographic structure; phase transformation,[6] texure,[26] and modification of lattice parameters due to ion implantation,[27] have been reported with the introduction of negative substrate bias.

Application of RF bias has also been extensively studied in growth of rock salt TiN-based films, which are structurally and electrically similar to the $Ti_xMo_{1-x}N$ films explored in this work. Sputtering of TiN_x with negative substrate bias prevented oxidation during growth to form stoichiometric TiN which resulted in higher hardness and elastic modulus in the absence of softer TiO_2.[30] It was also reported that higher adatom mobility due to high bias resulted in denser films by elimination of voids and the crystallographic orientation changed from (111) to (100). At high energy, the rock salt TiN_x grows with (100) texture along which the surface free energy is minimum,[31] whereas the most densely packed (111) plane is observed at lower bias.[32] The film orientation is generally expected to be determined by the planes that present the lowest sum of the surface energy, the strain energy, and the stopping potential.[33] There exists a critical thickness below which the surface energy term dominates resulting in (100) preferred orientation and the strain energy term dominates above this critical thickness which favors (111) oriented grains.[34] Zhao et al. demonstrated this theory experimentally with filtered arc deposited TiN films.[33] It was also reported that biasing the substrate for films below the critical thickness caused the preferred orientation to shift from (100) to (111). Conversely, films above the critical thickness are predominantly (111) oriented when unbiased and gradually change to (100) with increasing bias and eventually to (110) at very high bias (400 – 700 V),[33] at which point the stopping potential starts to dominate.

The plasma species,[25] ion energy, ion flux, and ion dosage govern the impact of substrate biasing on the film structure and properties.[18] As a result, the impact of RF substrate bias is material/process specific and straightforward predictions are difficult. These facts warrant further investigations into this field to better understand the behavior of substrate bias during plasma assisted deposition. In our previous work we have demonstrated that the stoichiometry of PEALD

$Ti_xMo_{1-x}N$ ($0 \leq x \leq 1$) can be tuned by varying the ratio of Ti and Mo precursor exposure.[15] In this study, we varied the RF substrate bias voltage during PEALD growth of $Ti_xMo_{1-x}N$, with equal number of exposures of Ti and Mo precursors that results in a Ti:Mo ratio of slightly greater than unity, henceforth referred to as TiMoN for simplicity. These PEALD TiMoN films with a range of RF substrate bias voltages were deposited on different substrates and the film structure, chemistry, and tribological properties are reported.

II. Experimental

A. PEALD Growth

A G2 Veeco-ALD Fiji system equipped with an optional substrate RF bias feature was used for the PEALD of TiMoN. Tetrakis(dimethylamido) titanium was used for the titanium precursor and bis(tert-butylimido)bis(dimethylamido)molybdenum[35] was used for the molybdenum precursor. The Fiji system allows for two reactor pumping techniques. For metal precursor pulsing the reactor turbo is bypassed to increase the reactor residence time providing a longer precursor/substrate interaction. Switching to turbo pumping mode for the plasma steps provides higher radical fluxes due to higher plasma densities and reduced radical recombination.

Alternating TiN and MoN deposition cycles in a 1:1 ratio was realized to obtain TiMoN composition. For the TiN cycle, the titanium precursor, heated to 75 °C, was pulsed in vapor draw mode for 0.25 seconds. Following a brief purge step, the TiN was completed with a 10 second, 300 W remote, inductively coupled N_2 plasma. The lower vapor pressure Mo precursor was delivered to the reactor via an optional precursor Boost™ technique that introduces a charge of Ar into the precursor cylinder prior to pulsing the precursor/Ar mix into the reactor. Each MoN

deposition cycle included three repetitions of the Mo precursor boosting process followed by a purge and then a 300 W N_2/H_2 (1/16) plasma for 40 seconds. Depositions were performed with a substrate temperature of 250 °C.

During each plasma step of the TiN and MoN cycles, following a one second stabilization, substrate bias, $|V_{bias}|$, was achieved by applying 13.56 MHz power to the substrate holder. The bias was left on until the end of each plasma step resulting in 9 seconds of bias for the TiN deposition and 39 seconds for the MoN. Voltages of $|V_{bias}| = 0$, 31, 62, 125, and 188 V were studied. See supplementary material (**Table S1**) at [URL will be inserted by AIP Publishing] for the entire deposition process reported in tabular form. Due to the requirements of the various analytical methods applied to the TiMoN films for this study, thinner and thicker films were deposited at each bias voltage except the 188 V, which suffered from an extremely small growth rate per cycle and only a thinner film was generated.

Substrates included silicon (100), silicon with thermal oxide (1000 nm), and c-plane sapphire. Substrates were placed on the substrate holder in the turbopumped load lock and maintained at $< 10^{-6}$ Torr for 30 minutes prior to loading into the reactor where they spent one hour prior to the start of the deposition process. When the deposition was finished, the samples were transferred from the reactor to the load lock for one hour of cooling prior to removal.

B. Ex-situ Spectroscopic Ellipsometry

Refractive index (n) and extinction coefficient (k) were measured on the films deposited on Si (100) substrate, with a Horiba UVISEL, utilizing a wavelength range of 225–886nm. The spectroscopic ellipsometry data were evaluated with a model combining a Drude term and two Lorentz oscillators. Only the thinner set of samples were analyzed with ellipsometry because the

thicker samples were sufficiently reflective to prevent light from penetrating to the underlying substrate.

C. XRR & XRD

A PANalytical Empyrean diffractometer with a Cu x-ray tube at a wavelength of 1.541 Å was utilized for x-ray reflectivity (XRR) and x-ray diffraction (XRD) measurements. A Bragg–Brentano HD mirror with soller slit, 4 mm mask, 1/8° divergence slit, and a 1/16° antiscatter slit was used for the incident beam for XRR measurement. The diffracted beam path used a 1/16° antiscatter slit, soller slit, and a PIXcel3D-Medipix3 1x1 area detector with 1 of 255 channels active with an active length of 0.055 mm. Gonio (symmetric) scans were performed with a step size of 0.005° (2θ) from 0° to 4° with a counting rate of 0.5 s/step. XRR data were fitted with X'Pert Reflectivity software (v 1.3a) with a layer model of a surface oxide on the ALD film above the substrate. Symmetric XRD measurements used a Bragg–Brentano HD mirror with appropriate slits and mask sizes to maximize irradiation of the incident beam without over irradiating the sample. A soller slit and 7.5 mm antiscatter slit were used on the diffracted beam path along with the PIXcel3D-Medipix3 1x1 area detector in scanning line 1D mode.

Bragg–Brentano HD mirror was utilized to condition the incident beam for grazing incidence XRD (Gi-XRD) measurement with a soller slit, 10 mm mask, 1/8° divergence slit, and a 1/8° antiscatter slit. The diffracted beam path utilized a soller slit, parallel plate collimator of 0.18° opening and a PIXcel3D-Medipix3 1x1 area detector. 2θ scans were taken keeping the incident angle ω fixed at an angle of 1° with respect to the film surface, with a step size of 0.04° and a counting rate of 0.55 s/step.

D. Four Point Probe

Film sheet resistance values were measured using a Lucas Labs 302 Resistivity Stand with a Keithley 2400 SourceMeter. Resistance measurements were taken on the films deposited on the Si-thermal oxide substrate. Film resistivity values reported are the product of the four point probe sheet resistance values and film thicknesses derived from the XRR fitting.

E. XPS

X-ray photoelectron spectroscopy (XPS) measurements were collected using a *Thermo* K-alpha system using monochromatic Aluminum K-α radiation with an excitation energy of 1486.7 eV and a hemispherical detector. High resolution scans were collected using a step size of 0.1 eV and an appropriate number of scans to achieve suitable signal to noise ratios. Compositional information was determined by fitting XPS data using relative sensitivity factors obtained from *Thermo* using *Thermo* Avantage 5.973 software. Peak locations were calibrated to the C1s peak energy for adventitious carbon at 284.8 eV. Samples were sputtered for 30s using 200 eV Ar^+ ion beam to remove surface contamination from air exposure.

F. Friction and Wear Testing

Friction and wear testing were performed to study the effects of varying RF bias voltage and substrate material on performance. Films were tested in a linear bi-directional reciprocating ball-on-flat configuration. A fixed 3 mm diameter ruby ball was mounted to a biaxial load cell to measure normal and friction forces. Wear and friction were monitored incrementally throughout the experiment by performing a stripe test, a method that preserves sections of the wear track at incremental sliding cycles to investigate the evolution of the wear behavior.[36,37] All samples underwent a total of 10,000 sliding cycles with a starting stroke length of 10 mm (20 mm total

cycle length). Stripe testing was performed with cycle intervals of 500, 1k, 1.5k, 3k, 5k, with stroke lengths of 10, 8, 6, 4, and 2 mm respectively.

Prior to testing, samples and ruby counter-samples were rinsed with methanol and allowed to dry. Samples were tested in lab air with a RH of 30 ± 5%. A normal load of 0.1 N and a sliding speed of 1 mm/s were applied corresponding to a max Hertzian contact pressure of 820 MPa. Wear volume of each cycle interval was determined from the worn surface topographies measured with a scanning white-light optical profilometer (Bruker Contour GT, Billerica, MA). Five line scans (10 per stripe region) for each worn surface profile were individually analyzed to assess the cross-sectional area of the wear scar[38]. Wear Rate (***K*** [mm^3/(Nm)]) shown in Eq. 1 is the volume lost (***V*** [mm^3]) per unit normal load (***F***$_N$ [N]) multiplied by sliding distance (***d*** [m]). Wear rate is determined by calculating the average measured worn cross-sectional area, A [mm^2], divided by the product of the applied normal load F_N and the number of a total sliding cycles N, (1 cycle=2 sliding passes, s):

$$K[mm^3/Nm] = \frac{V[mm^3]}{F_N[N]d[m]} = \frac{1000[mm/m]A[mm^2]s[m]}{2F_N[N]C[cycles]s[\frac{m}{cycle}]} = \frac{1000A}{2F_NC} \quad (1)$$

Friction coefficient was calculated by dividing the frictional force over the normal force. Average friction coefficient was calculated incrementally every 500 cycles of sliding.

G. Roughness Measurements

Roughness measurements on TiMoN thick films were performed on a Bruker Dimension Icon atomic force microscope (AFM) (Bruker, Billerica, MA, USA). The surface topography was measured using a sharp triangular silicon nitride cantilever, ScanAsyst-Air, with a radius of ~ 2

nm. The data were collected at 1 Hz rate in PeakForce mode. The RMS and Ra values were determined using NanoScope Analysis software v 2.0 (Bruker, Billerica, MA, USA).

III. Results and Discussion

A. PEALD Growth

TiMoN films grown on Si (100) substrates received a varying negative RF substrate bias magnitude, $|V_{bias}|$, ranging from 0 to 188 V. The growth per cycle (GPC) is defined here as the average increase in thickness (derived from the XRR fitting) per metal (or N plasma) exposure (**Figure 1)**. Two sample sets, hereto referred to as *thick* and *thin*, were analyzed and both had identical growth parameters except for the total number of ALD cycles. The thin set was grown with 444 total metal precursor pulses, whereas the number of cycles for the thick samples were adjusted to keep the thickness ~70 nm (0 V = 1332, 31 & 62 V = 1100 and 125 V = 2200 cycles). Films grown on the unbiased substrates had growth rates (~0.5 Å/cycle) similar to the previously reported case that were grown in similar method.[15,18] Introducing RF substrate bias increased the GPCs to a maximum at $|V_{bias}|$ = 31 – 62 V, possibly due to nucleation of voids or gas bubbles by impingement of high energy ion species.[22,29] Further increases in $|V_{bias}|$ caused the growth rate to decrease, which can be explained by sputtering of deposited atoms by incoming ions with excessive energy brought about by the high bias voltage.[39–42] Note that the film thickness at $|V_{bias}|$ = 188 V was only 2.7 nm for 444 ALD cycles giving a very low GPC of 0.06 Å/cycle. This low sample thickness is not ideal for XRD or XPS analysis, so this sample is not discussed in the following analyses.

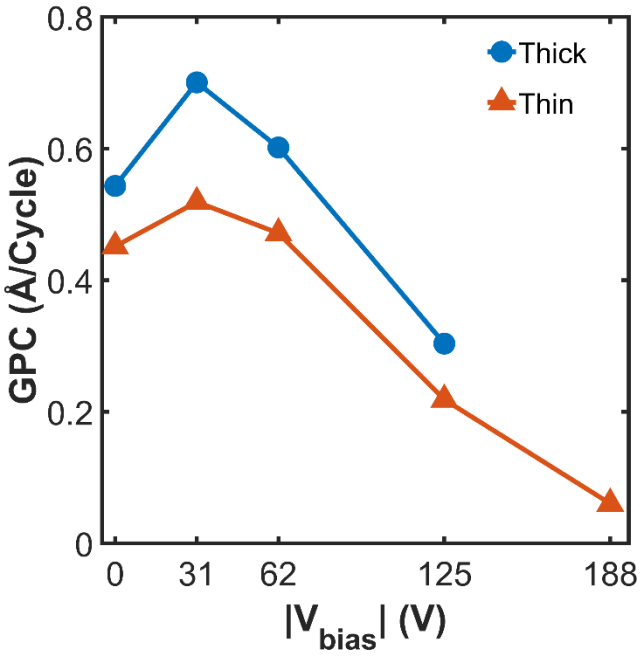

FIG. 1. Growth per cycle (GPC) in Å/cycle of thick (67-78 nm) and thin (10-23 nm) samples set of TiMoN on Si for a range of RF substrate bias voltage magnitudes. The GPCs were calculated using the final film thickness estimated from XRR fitting.

B. Composition

XPS was used to measure the composition of samples grown on silicon substrates. Compositional data are shown in **Figure 2**, where a number of trends emerge from increasing substrate bias. Overall, N content increases with increasing substrate bias, while both Ti and Mo content decreases, resulting in an increasing N:Metal ratio from 0.9 to 1.01 and decreasing Ti:Mo ratio from 1.9 to 1.5, shown in the right axis of **Figure 2a**. These data indicate an increased incorporation of MoN at higher substrate biases, although the films are still Ti rich relative to the (1:1) pulse ratio. Data from 188V substrate bias was omitted, as those films were too thin for reliable XPS quantification of the bulk material. Overall, TiMoN films deposited at all substrate biases exhibit oxygen contamination below 2.5% and carbon contamination below 2% (**Figure**

2b). Our ALD reactor is equipped with a fused silica ("quartz") based ICP source which could act as a source for the oxygen contamination.

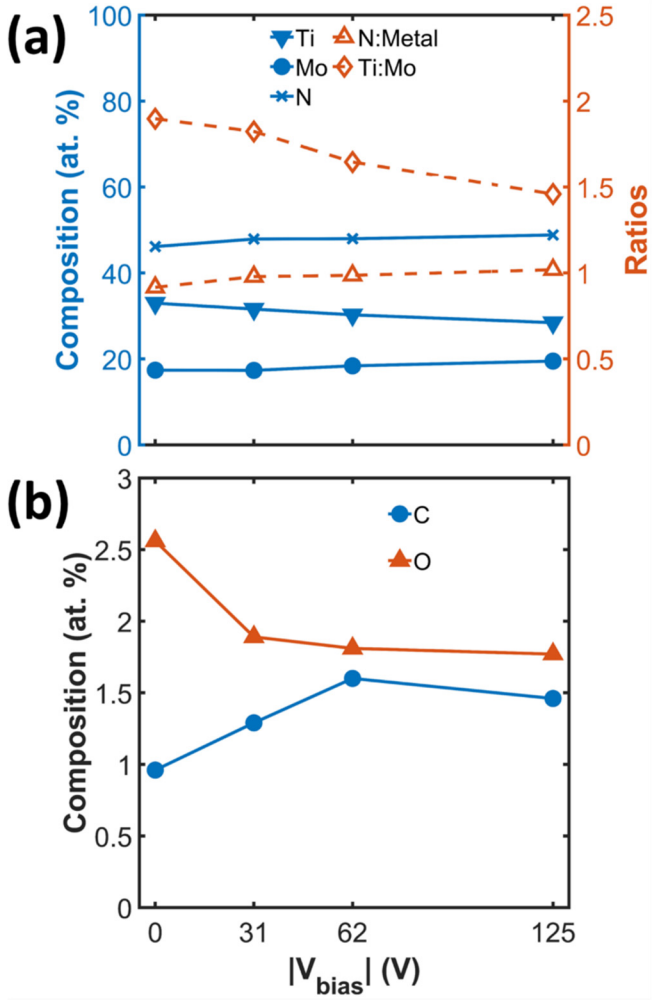

FIG. 2. XPS derived (a) composition in atomic percentage along with N:Metal and Ti:Mo ratios, and (b) impurity concentration (carbon and oxygen) in atomic percentage as a function of $|V_{bias}|$.

High resolution XPS spectra (**Figure 3**), indicate negligible changes to the chemical binding environment of the constituent elements for up to $|V_{bias}|$ = 125V. The Ti2p region exhibits a doublet at 455.5 eV with $2p_{3/2}$ and $2p_{1/2}$ separated by 6 eV, along with the associated shakeup peaks, both indicative of Ti^{3+}. The Mo3d region exhibits two doublets, one at 228.8 eV with $3d_{5/2}$ and $3d_{3/2}$ separated by 3.2 eV associated with Mo^{3+}, and a second at 230.0 eV with $3d_{5/2}$ and $3d_{3/2}$

separated by 3.4 eV associated with the shakeup peaks. These features are consistent with a bonding environment of mixed ternary Mo-Ti oxides and nitrides.[43] Specific peak fits are not shown for clarity to better compare the constituent XPS spectra; for a more comprehensive treatment of the analysis and fitting see our previous publication.[15] The O1s peak location is consistent with a mixed TiO_2-MoO_3 surface oxide, while the C1s peak exhibits carbide bonding at 282.7 eV. At $|V_{bias}|$ = 188 V, significant chemical changes are seen in the XPS data, although due to the low growth rate (as determined by XRR) at 188V we assign these chemical species to those at the TiMoN-SiO_2 film-substrate interface and not representative of the bulk of the films. Formation of TiON and additional TiO_2 species are evidenced by the Ti2p and O1s high regions, while formation of pyrrolic N species is indicated in the N1s high resolution spectrum, consistent with the higher nitrogen content for films deposited at 188 V. As Ti is more electropositive than Mo, it would be expected to preferentially bond with O species at the SiO_2 substrate interface, forming this TiON bonding, while the pyrrolic N is likely formed from energetic radicals impinging on the sample surface.[44]

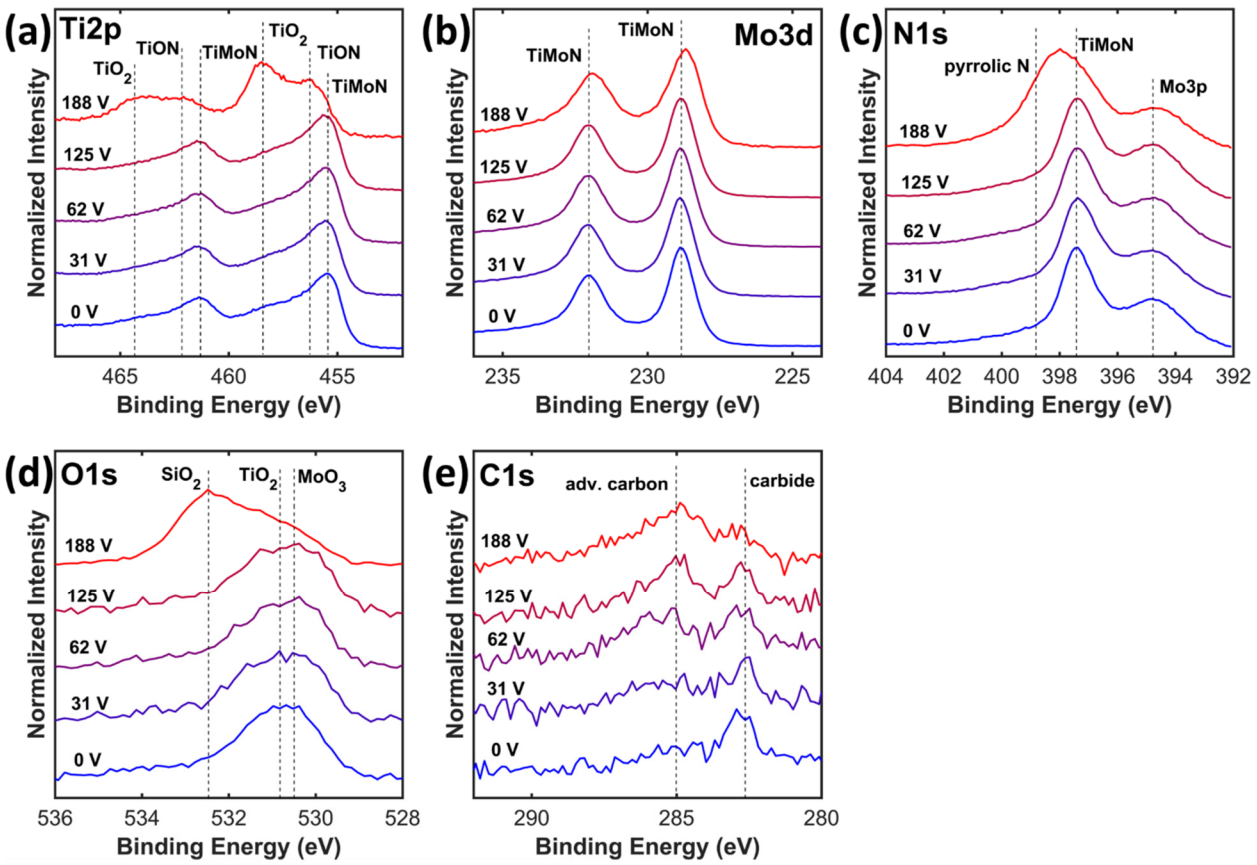

FIG. 3. High resolution a) Ti2p; b) Mo3d; c) N1s; d) O1s; e) C1s XPS spectra of TiMoN grown on Si as a function of $|V_{bias}|$.

C. Crystal Structure

Both the thick and thin films grown on Si (100) substrates showed evidence of crystallinity at all $|V_{bias}|$ in grazing incidence x-ray diffraction (Gi-XRD) measurements (**Figure 4)**. Well defined Bragg peaks were observed near 36°, 42° and 62° 2θ corresponding to (111), (200) and (220) of FCC rock salt structure. Weak reflections from (311), (222), (400), (331) and (420) planes of the FCC structure were also observed near 73°, 77°, 92°, 104.5° and 108.5° respectively. All the peak positions were found to be at an intermediate location between the cubic TiN (00-038-1420) and cubic MoN (01-079-5757), indicating solid solution between rock salt TiN and MoN.

The larger Mo atom substituted the Ti atom in the FCC rock salt structure of TiN decreases the 2θ values of the Bragg reflections.[10,15]

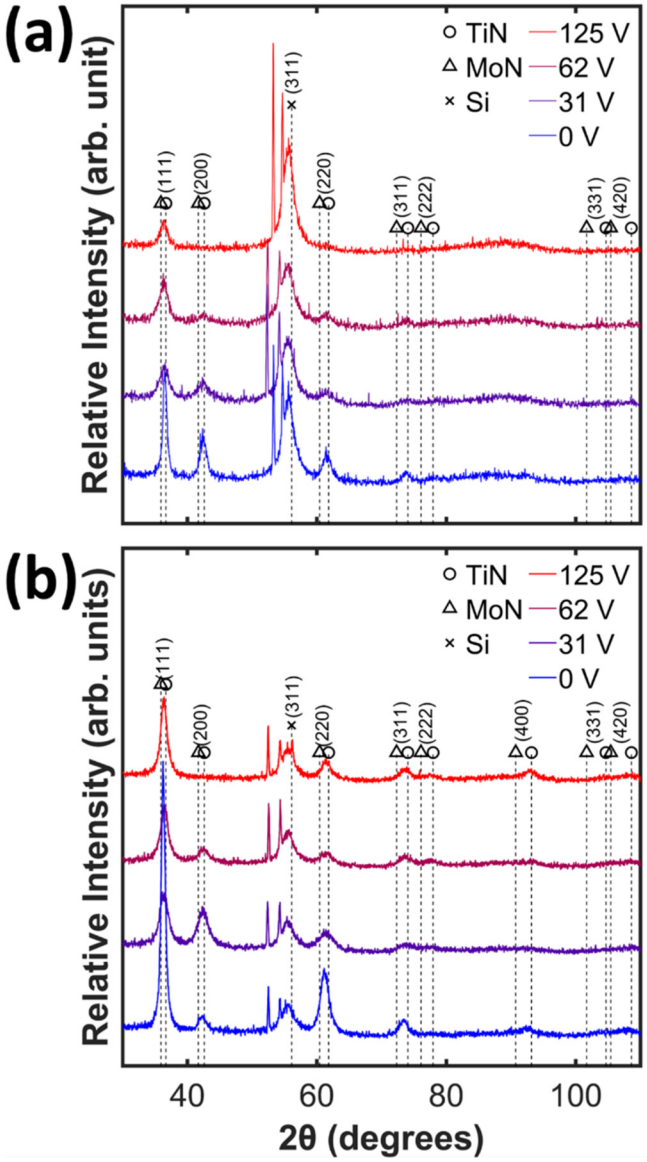

FIG. 4. Grazing incident x-ray diffraction, with incident angle fixed at 1°, of (a) thin and (b) thick TiMoN on Si substrate as a function of $|V_{bias}|$.

Preferred crystallographic orientation plays an important role in the wear performance of TiN based coatings.[45] TiN films with a (111) textured are known to have excellent wear and abrasion properties.[46] We define the Bragg peak intensity fraction, N_{hkl}, as the ratio of the

integrated intensity, I_{hkl}, of the corresponding Bragg peak over the sum of the integrated intensity of (111), (200) and (220) reflections of symmetric θ-2θ XRD scan taken on the thick TiMoN samples deposited on Si substrate. See supplementary material at [URL will be inserted by AIP Publishing] for the θ-2θ XRD scans (**Figure S1**) and the I_{hkl} and N_{hkl} (**Table S2**) at various $|V_{bias}|$. A plot of N_{hkl} against $|V_{bias}|$ shows that the unbiased film was almost entirely (111) oriented (**Figure 5a**). An increase of N_{200} was seen at $|V_{bias}|$ of 31 V, where equal proportion of (111) and (200) oriented grains were found. Similar changes in orientation with increasing RF bias (from (111) to (200)) were observed for sputtered TiN[30] and for ~75 nm HfN_x films grown by PEALD.[22] Increasing the $|V_{bias}|$ to 62 V caused the N_{111} to decrease to a minimum and the N_{200} decreased to zero. The N_{220} increased for the 62 V sample. Similar appearance of preferred (220) preferred orientation has also been reported for filtered arc deposited TiN at very high negative substrate bias.[33] Further increasing the $|V_{bias}|$ to 125 V did not change the preferred orientation significantly compared to what was found at 62 V.

The texture of a deposited film can be influenced by the growth process,[47] substrate structure,[46] and the film thickness.[34] Studies showed that the evaporation ion plated TiN grows with (111) texture whereas the magnetron-sputtered ones have moderate (100) and (110) texture.[47] Thermodynamically speaking, minimization of the total energy of crystal planes dictates the crystallographic orientation. Although, the surface energy is minimum for (100) plane in rock salt structure,[33,34] the strain energy is minimum for (111) plane.[34,48] The strain energy increases linearly with the film thickness while the surface energy remains independent. As a result, at lower film thickness surface energy term dominates making the film (100) oriented, while the orientation along (111) and (110) is expected at higher film thickness.[46] Therefore a critical thickness exists above which the strain energy dominates over the surface energy. In this study we did not

investigate the critical thickness explicitly, but the dominance of strain energy for thick samples and surface energy for thin samples suggests that the critical thickness for this system lies somewhere between these two thicknesses (20 nm and 70 nm). In terms of experimentally specified parameters, the preferential orientation of the films is a complex function of film thickness and RF bias.

The average lattice parameter was calculated considering cubic unit cell from all the observable Bragg peaks in the Gi-XRD data (**Figure 5b**). The boxplots represent the spread of lattice parameters obtained from different crystal planes. The theoretical unit cell dimensions shown in the figure were calculated considering a solid solution of cubic TiN and MoN using the XPS-derived composition. The lattice parameters were similar to, but slightly less than, the expected values based on the chemical compositions. The changes in the lattice parameter found were not significant with the increase in bias voltages or the film thickness. The apparent crystallite sizes were calculated from Scherrer broadening of the (111) Bragg peak as we have done previously.[12,15,49] The films were nanocrystalline (~12.5 nm) on the unbiased substrates (**Figure 5c**). With introduction of bias voltage, the crystallite size decreased to about half and did not change significantly with increasing bias or film thickness. The growth of crystallites are likely disrupted by the bombardment of high energy ions causing continuous re-nucleation,[26,28,29] resulting in finer grains with the introduction of bias voltages. The crystallite sizes estimated from Scherrer broadening here is also consistent with the finding from cross-sectional TEM imaging. See supplementary material at [URL will be inserted by AIP Publishing] for cross-sectional TEM image (**Figure S2**) showing the crystallite size of TiMoN deposited at 31 V.

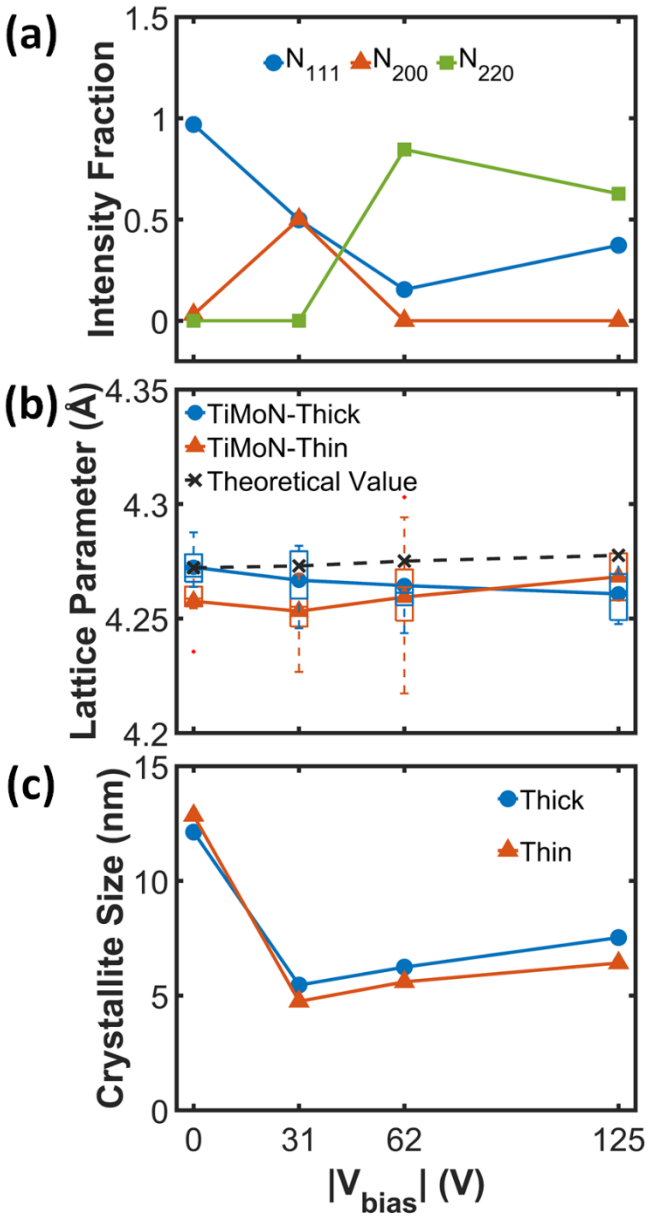

FIG. 5. (a) Bragg peak intensity fraction showing preferred orientation of thick TiMoN deposited on Si substrate, derived from symmetric θ-2θ XRD measurement. (b) Lattice parameter of both thick and thin films with the theoretical unit cell dimensions considering solid solution of cubic TiN and MoN, and (c) crystallite sizes calculated using Debye Scherrer equation, considering crystallite size to be the only source of peak broadening, form the Gi-XRD data of TiMoN on Si with respect to $|V_{bias}|$.

D. Physical Properties: Electrical Resistivity & Density

Low electrical resistivities (672 μΩ-cm) were found for films deposited on unbiased Si-thermal oxide substrates as determined by four-point probe measurements (**Figure 6a**). Similar results (712 μΩ-cm) were observed previously under identical growth conditions.[15] The resistivities almost doubled with introduction of $|V_{bias}|$ and did not change significantly with further increases in bias magnitude. For thin films with such low impurity concentration, the electrical resistivity is governed by the limitation of mean free path of the charge carriers due to grain boundary scattering.[50] Reduced grain size with $|V_{bias}|$ (**Figure 5c**) provides a large volume of grain boundaries which contributes to the grain boundary scattering and thus may be responsible for the higher resistivity. PEALD TiN showed a similar increase in resistivity due to reduced grain size.[50–52]

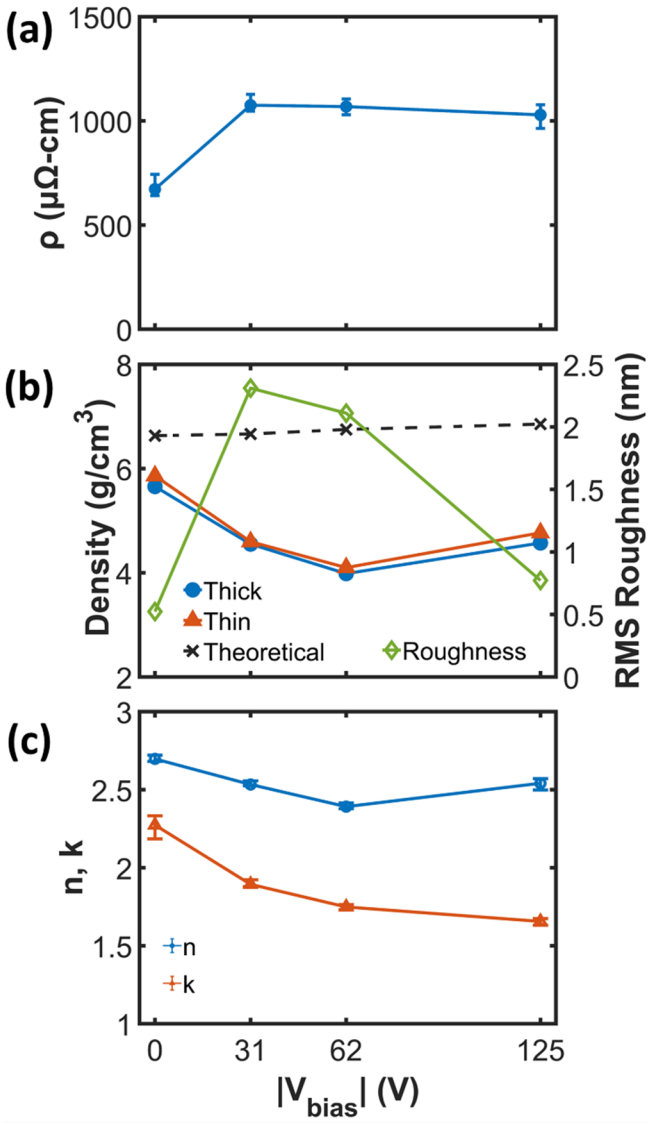

FIG. 6. (a) Changes in electrical resistivity of the thin (10-23 nm) TiMoN on Si-thermal oxide substrate with respect to $|V_{bias}|$. (b) XRR derived density of both thick and thin TiMoN films on Si and the theoretical density estimated from XPS composition considering solid solution of cubic TiN and MoN. The RMS roughnesses from AFM measurements are shown on the right y-axis. (c) Refractive index (n) and extinction coefficient (k) of the thin sample set with respect to $|V_{bias}|$.

The highest density was observed for the unbiased films as determined by the XRR derived density (**Figure 6b**). Similar densities were observed for PEALD $Ti_xMo_{1-x}N$[15] and TiN[52] deposited with Ar added N_2 plasma. Introducing RF substrate bias voltages caused a drop in density possibly

due to the void generation in addition to the reduction in grain sizes. Grain size decreased almost 50%, increasing the volume of grain boundaries, which may also contribute to density decreases. Densification at higher $|V_{bias}|$ is observed which can be explained by eliminations of voids by higher adatom mobility.[28,29] Note that the initial decrease in density is larger than the subsequent rise at higher $|V_{bias}|$. This observation may be explained in that the initial decrease is due to the combination of void generation and reduction in grain sizes, but the grain sizes did not change at higher $|V_{bias}|$ and the increase in density may be due to the elimination of voids. At all bias conditions the film densities were significantly lower than the theoretical bulk density, estimated from the cubic unit cell of TiN (00-038-1420) and MoN (01-079-5757) considering a solid solution based on the XPS derived compositions. This deviation from the theoretical density could result from the large number of grain boundaries from the nanocrystalline grains, impurities, and the possible existence of amorphous regions.

The RMS roughness of the films deposited on Si substrate were determined by atomic force microscopy, shown on the right axis of **Figure 6b**. See supplementary material at [URL will be inserted by AIP Publishing] for AFM images used for RMS calculation (**Figure S3**) and the Ra and RMS roughness as a function of $|V_{bias}|$ (**Figure S4**). The initial increase in roughness with $|V_{bias}|$ can be attributed to the voids generated by high energy ion impingement that appears as roughness on the surface. The smoother film found at $|V_{bias}|$=125 V may be attributed to the filling up the valleys of the columnar grains on the surface by higher adatom mobility[8,24,28] and possibly due to preferential sputtering of the peaks of the columnar grains by high energy ion bombardment. The roughness of the films deposited on Si-thermal oxide (data not shown) were very similar to the ones shown for the films on Si (100).

E. Optical Properties: Refractive Index (n) & Extinction Coefficient (k)

The refractive index, *n*, and extinction coefficient, *k*, (reported at 633 nm) for the thin deposition samples are shown in **Figure 6c**. Both *n* and *k* decrease slightly with increasing bias 0 – 62V. While *k* continues to decrease at the bias is further increased to 125V, *n* showed a slight increase. A root cause for the variations in optical properties is not obvious with stoichiometry, impurities, density, and crystallinity variations all potentially contributing. It is to be noted that the changes in *n* with $|V_{bias}|$ follows the trend for density very closely as is expected. The *n* and *k* values are reasonable intermediate values of the previously reported pure TiN (*n*: 1.2, *k*: 2.3)[53] and MoN (*n*: 3.6, *k*: 3.3)[35] values.

F. Film Stress

The lattice strain for the thick polycrystalline TiMoN films were estimated from Gi-XRD data and was used to calculate the film stress using $\sin^2 \psi$ method.[54] The Elastic modulus (E) and the Poisson's ratio (ν) were approximated to the values for TiN (E = 447 GPa & ν = 0.2),[55] for the biaxial stress model. The film stresses at all bias voltages were found to be compressive between 3.5 and 4.4 GPa (**Figure 7**). The compressive stress in the unbiased film (3.5 GPa) was consistent with previously reported stress of PEALD $Ti_xMo_{1-x}N$.[15] With increasing bias magnitude the film stress did not change considerably.

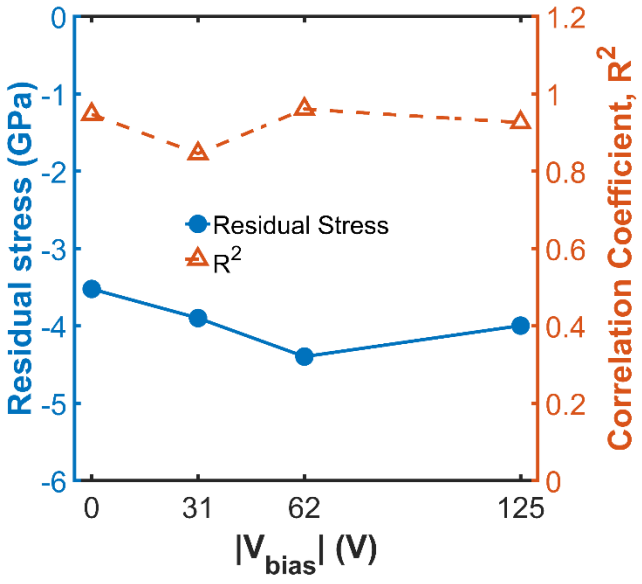

FIG. 7. Residual stress of thick TiMoN films on Si (100) substrate, calculated using $\sin^2\psi$ method from the lattice distortion measured by XRD at grazing incident geometry.

G. Friction and Wear

The lowest total wear rates and friction coefficients were observed for films with the lowest $|V_{bias}|$ (**Figure 8**). TiMoN films deposited on both Si (100) and Si-thermal oxide with a $|V_{bias}|$ of 0 V achieved the lowest total wear rates (1 x 10^{-6} mm^3/Nm). All films with applied bias voltage delaminated or wore through to the substrate prior to the completion of 10k sliding cycles. The film failure point becomes clearer in (**Figure 9**), where the average friction coefficient is plotted over the total number of cycles; average friction was calculated incrementally every 500 cycles of sliding and error bars represent the standard deviation of the measured friction coefficient during the 500 cycles increment. The transition to high friction coefficients ($\mu>0.5$) are indicative of large-scale film delamination, subsequently resulting in sliding on the substrate. Very large error bars represent significant fluctuations in friction coefficient that can be correlated to film failure or interrupted sections of intact film and delaminated regions. Film delamination was confirmed using SEM imaging and EDS of the wear track, bulk film, and delaminated regions. See

supplementary material at [URL will be inserted by AIP Publishing] for SEM images (**Figure S5-7**), EDS spectra (**Figure S8-11**) and EDS compositions (**Table S3)** inside and outside the wear scar.

The friction coefficients of films on Si with any applied $|V_{bias}|$ become larger than 0.4 after 1500 sliding cycles which corresponds to an increase in wear rate **(Figure 8a**). The sample with $|V_{bias}|$ = 125 V reached extremely high wear after few sliding cycles and wear rates were not recorded after 5k cycles because the film had completely worn away. The 31 and 62 V films had comparable friction coefficients to the 125 V sample after 3k sliding cycles but had surprisingly low friction coefficients and wear rates below 2k cycles. The 31 V sample had the lowest wear after 1k cycles while the wear behavior of the 62 V and 0 V samples performed similarly until 3k cycles wherein the 62 V sample experienced failure from delamination. This could indicate that the 31 and 62 V samples are more wear resistant but have worse adhesion to the Si substrate. Similar trends in the coatings deposited on Si were observed for TiMoN films on Si-thermal oxide. The total wear of the 0 V sample continues to decrease over the total sliding cycles and achieves a similar wear rate to that of the comparable film on Si. The 31 and 62 V samples approached similar wear rates to the 0 V sample up until 3k cycles and then began to increase with continued sliding. On both substrates, the 31 V sample was initially more wear resistant than the 0 V sample but suffered delamination with prolonged sliding.

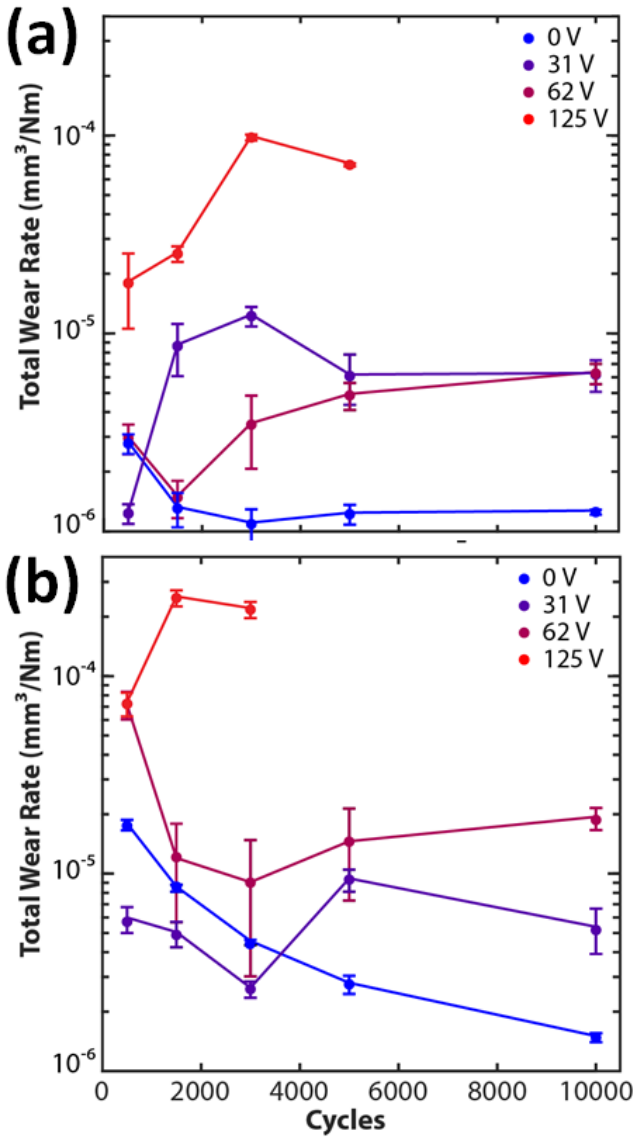

FIG. 8. Total wear rate of TiMoN on (a) Si and (b) Si-thermal oxide substrates with varying $|V_{bias}|$.

The change in film characteristics with increasing voltage bias, such as increasing (111) orientation, decreasing grain size, and increasing compressive film stresses, have been shown to result in improved wear characteristics of mixed-metal nitride films when they are also accompanied by increased density.[56] In the present study, the long-term wear durability of ALD mixed-metal nitrides decreases with increasing bias voltage, which is opposite of what has been reported in more traditional sputtering deposition methods with bias voltage. Experiments at higher

bias voltages tended to delaminate. There may be a competition between film delamination and film wear, as indicated by the 31 and 62 V samples that tend to delaminate yet have improved wear performance in the early stages. In several studies, there is a certain point at higher bias voltages that result in reduced adhesion due to low densification and/or high compressive stress.[56] Such behavior is consistent with the 125 V sample in our study. At this point, we can only speculate the root of the decrease in long-term wear performance (which includes wear and delamination) with increasing bias voltage. Low density porous films could lead to decreased wear performance at higher $|V_{bias}|$.

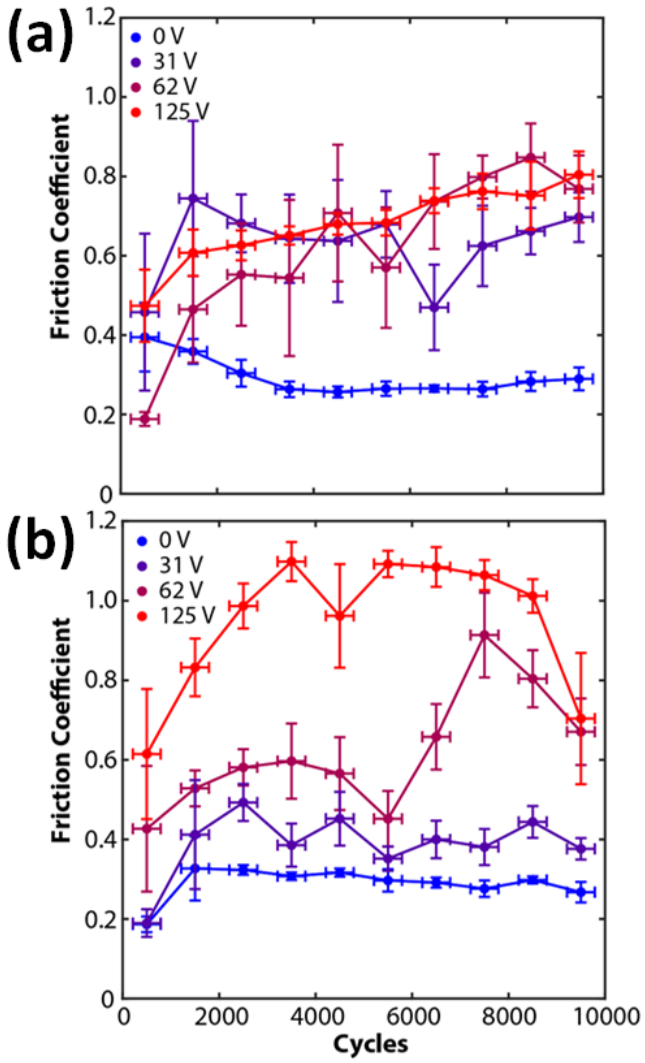

FIG. 9. Friction coefficient of TiMoN on (a) Si and (b) Si-thermal oxide substrates with varying $|V_{bias}|$.

H. Epitaxial Growth: Structure & Symmetry

Films were also deposited on c-plane sapphire substrates to examine the influence of crystalline template upon film structure. These films grew epitaxially in [111] direction on the (0001) plane of the sapphire as evident from the $\theta - 2\theta$ XRD scan (**Figure 10a)**. At $|V_{bias}|$ = 125 V, some grains oriented towards [220] direction were found as a weak reflection at 62° 2θ. Such changes in orientation at very high bias voltages due to dominance of stopping potential were

previously demonstrated for filtered arc deposited TiN films.[33] Increase in FWHM of the (111) Bragg peak with introduction of bias suggests deterioration of structural coherence (**Figure 10a – inset**). Further increase in bias resulted in narrower Bragg peak and longer length of structural coherence consistent with the non-monotonic changes in other properties such as density, conductivity, as well as the FWHM in the non-epitaxial samples.

The rotational (azimuthal, ϕ) scans of asymmetric (020) planes of the epitaxial films showed peaks at every 60° (**Figure 10b**). Based on the rock salt structure, azimuthal scans of the (020) planes are expected to yield peaks with 120° separation.[57] The observation here of 60 separation indicates that the film contains two domains rotated at 60° relative to each other, as demonstrated previously by similar ϕ scans and electron backscatter diffraction for (111) epitaxial rock salt MgO on GaN.[57] (111) oriented epitaxial rock salt cubic ScN on hexagonal GaN substrate has also shown similar six-fold rotational symmetry due to cubic-twined nature.[58] The weak intensity for $|V_{bias}|$ = 125 V samples relative to the unbiased films were possibly due to smaller domain sizes. The finer domain size can be explained by continuous re-nucleation by bombardment of high energy ions at higher bias.[26,28] The GPC and density derived from XRR for the epitaxial films were comparable to the polycrystalline films grown on Si (100) substrate (data not shown).

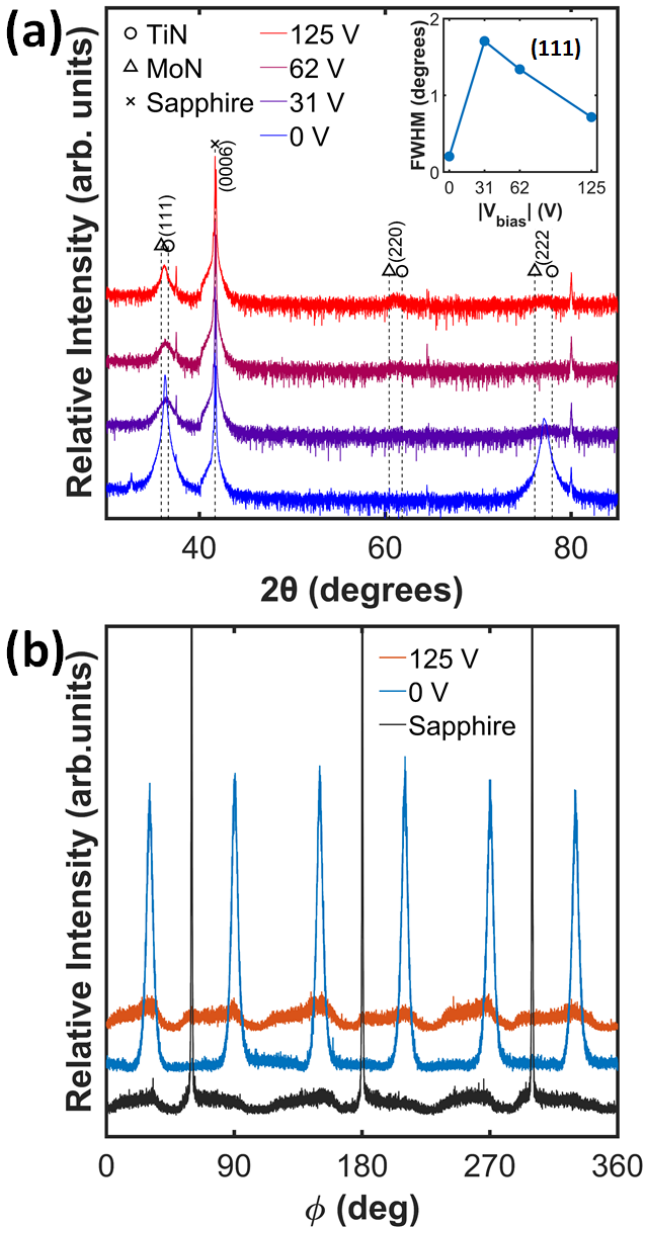

FIG. 10. (a) θ-2θ scan of TiMoN on c-plane sapphire as a function of $|V_{bias}|$ and FWHM of the (111) peak as a function of $|V_{bias}|$ in the inset. (b) ϕ rotational scans of (002) planes of epitaxial TiMoN on sapphire substrate at 125 V (orange) and 0 V (blue) $|V_{bias}|$ shown in comparison to the $(10\bar{1}4)$ of the sapphire substrate (black).

IV. Conclusion

TiMoN films deposited by PEALD at 250 °C resulted in nanocrystalline films that appeared to incorporate voids/porosity and result in lower film density with introduction of negative RF substrate bias voltage. At high $|V_{bias}|$ the deposited films were resputtered by the bombardment of incoming energetic ions causing lower GPCs. Introduction of $|V_{bias}|$ also caused continuous re-nucleation resulting in smaller grains that may have caused higher electrical resistivity of the films due to the increased scattering of carriers from the large number of grain boundaries. The FCC rock salt polycrystalline films grown on Si and Si-thermal oxide substrates had (111) preferred orientation at lower $|V_{bias}|$ which changed to (110) at higher $|V_{bias}|$. The residual stress in the film were compressive and did not change significantly with $|V_{bias}|$. Delamination of films and high wear rates were observed at high $|V_{bias}|$ possibly due to void filled, low-density films. Epitaxial films deposited on c-plane sapphire substrate showed (111) orientation with twinned domains rotated at 60° to each other. With increasing $|V_{bias}|$ the crystal quality of the epitaxial films deteriorated possibly due to reduced size of the twinned domains by continuous re-nucleation by high energy ions.

ACKNOWLEDGMENTS

All the authors acknowledge the National Science Foundation for providing fund for this research through the project NSF No. CMMI #1826251. This material is based upon work supported by the National Science Foundation Graduate Research Fellowship Program under Grant #1449440 (Van Meter) and #1842163 (Babuska). All the authors also acknowledge Dr. Yan Xin from National

High Magnetic Field Laboratory Tallahassee, FL, 32309, for the TEM measurements taken in this research.

DATA AVAILABILITY STATEMENT

The data that support the findings of this study are available from the corresponding author upon reasonable request.

REFERENCES

[1] M. Hua, H.Y. Tam, H.Y. Ma, and C.K. Mok, Wear **260**, 1153 (2006).

[2] X. Peng, C. Pi, X. Zhang, S. Li, K. Huo, and P.K. Chu, Sustain. Energy Fuels **3**, 366 (2019).

[3] R. Ramesh, D.K. Nandi, T.H. Kim, T. Cheon, J. Oh, and S.-H.H. Kim, ACS Appl. Mater. Interfaces **11**, 17321 (2019).

[4] N.S. Lawand, H. van Zeijl, P.J. French, J.J. Briaire, and J.H.M. Frijns, in *2013 IEEE SENSORS* (IEEE, 2013), pp. 1–4.

[5] E. Vancoille, J.P. Celis, and J.R. Roos, Wear **165**, 41 (1993).

[6] M. Pfeiler, K. Kutschej, M. Penoy, C. Michotte, C. Mitterer, and M. Kathrein, Surf. Coatings Technol. **202**, 1050 (2007).

[7] Q. Yang, L.R. Zhao, P.C. Patnaik, and X.T. Zeng, Wear **261**, 119 (2006).

[8] K.M. Calamba, I.C. Schramm, M.P. Johansson Jõesaar, J. Ghanbaja, J.F. Pierson, F. Mücklich,

and M. Odén, J. Appl. Phys. **122**, 065301 (2017).

[9] A. Joshi and H.S. Hu, Surf. Coatings Technol. **76**–**77**, 499 (1995).

[10] J.W. Jeon, S.G. Hong, K.R.H.R. Kim, and K.R.H.R. Kim, J. Vac. Sci. Technol. A Vacuum, Surfaces, Film. **26**, 140 (2008).

[11] J. Xu, H. Ju, and L. Yu, Vacuum **110**, 47 (2014).

[12] M.J. Sowa, L. Ju, A.C. Kozen, N.C. Strandwitz, G. Zeng, T.F. Babuska, Z. Hsain, and B.A. Krick, J. Vac. Sci. Technol. A **36**, 06A103 (2018).

[13] Y.-Y. Chang, H. Chang, L.-J. Jhao, and C.-C. Chuang, Surf. Coatings Technol. **350**, 1071 (2018).

[14] J. Xu, H. Ju, and L. Yu, Jinshu Xuebao/Acta Metall. Sin. **48**, 1132 (2012).

[15] M.I. Chowdhury, M. Sowa, A.C. Kozen, B.A. Krick, J. Haik, T.F. Babuska, and N.C. Strandwitz, J. Vac. Sci. Technol. A **39**, 012407 (2021).

[16] W. Lenguaer and P. Ettmayer, Mater. Sci. Eng. A **105**–**106**, 257 (1988).

[17] F. Regent and J. Musil, Surf. Coatings Technol. **142**–**144**, 146 (2001).

[18] T. Faraz, H.C.M. Knoops, M.A. Verheijen, C.A.A. van Helvoirt, S. Karwal, A. Sharma, V. Beladiya, A. Szeghalmi, D.M. Hausmann, J. Henri, M. Creatore, and W.M.M. Kessels, ACS Appl. Mater. Interfaces **10**, 13158 (2018).

[19] T. Faraz, K. Arts, S. Karwal, H.C.M. Knoops, and W.M.M. Kessels, Plasma Sources Sci. Technol. **28**, 024002 (2019).

[20] M. Legallais, H. Mehdi, S. David, F. Bassani, S. Labau, B. Pelissier, T. Baron, E. Martinez, G.

Ghibaudo, and B. Salem, ACS Appl. Mater. Interfaces **12**, 39870 (2020).

[21] S. Belahcen, C. Vallée, A. Bsiesy, A. Chaker, M. Jaffal, T. Yeghoyan, and M. Bonvalot, J. Vac. Sci. Technol. A **39**, 012410 (2021).

[22] S. Karwal, M.A. Verheijen, B.L. Williams, T. Faraz, W.M.M. Kessels, and M. Creatore, J. Mater. Chem. C **6**, 3917 (2018).

[23] S. Karwal, M.A. Verheijen, K. Arts, T. Faraz, W.M.M. Kessels, and M. Creatore, Plasma Chem. Plasma Process. **40**, 697 (2020).

[24] J.E. Sundgren, B.O. Johansson, and S.E. Karlsson, Thin Solid Films **80**, 77 (1981).

[25] H. Ljungcrantz, L. Hultman, J. -E. Sundgren, and L. Karlsson, J. Appl. Phys. **78**, 832 (1995).

[26] I. Petrov, P.B. Barna, L. Hultman, and J.E. Greene, J. Vac. Sci. Technol. A Vacuum, Surfaces, Film. **21**, S117 (2003).

[27] Y. Igasaki and H. Mitsuhashi, Thin Solid Films **70**, 17 (1980).

[28] P.-K. Huang and J.-W. Yeh, J. Phys. D. Appl. Phys. **42**, 115401 (2009).

[29] I. Petrov, L. Hultman, J. -E. Sundgren, and J.E. Greene, J. Vac. Sci. Technol. A Vacuum, Surfaces, Film. **10**, 265 (1992).

[30] P. Patsalas, C. Charitidis, and S. Logothetidis, Surf. Coatings Technol. **125**, 335 (2000).

[31] Thomas F. Kuech, *Handbook of Crystal Growth* (Elsevier, 2015).

[32] G. Knuyt, C. Quaeyhaegens, J. D'Haen, and L.M. Stals, Thin Solid Films **258**, 159 (1995).

[33] J.P. Zhao, X. Wang, Z.Y. Chen, S.Q. Yang, T.S. Shi, and X.H. Liu, J. Phys. D. Appl. Phys. **30**, 5 (1997).

[34] J. Pelleg, L.Z. Zevin, S. Lungo, and N. Croitoru, Thin Solid Films **197**, 117 (1991).

[35] A. Bertuch, B.D. Keller, N. Ferralis, J.C. Grossman, and G. Sundaram, J. Vac. Sci. Technol. A Vacuum, Surfaces, Film. **35**, 01B141 (2017).

[36] A.A. Pitenis, K.L. Harris, C.P. Junk, G.S. Blackman, • W Gregory Sawyer, and B.A. Krick, (n.d.).

[37] J.M. Urueã, A.A. Pitenis, K.L. Harris, and W.G. Sawyer, Tribol. Lett. **57**, 1 (2015).

[38] Z. Hsain, G. Zeng, N.C. Strandwitz, and B.A. Krick, Wear **372**–**373**, 139 (2017).

[39] H. Hajihoseini, M. Kateb, S. Ingvarsson, and J.T. Gudmundsson, Thin Solid Films **663**, 126 (2018).

[40] Q. Kong, L. Ji, H. Li, X. Liu, Y. Wang, J. Chen, and H. Zhou, Mater. Sci. Eng. B Solid-State Mater. Adv. Technol. **176**, 850 (2011).

[41] D.M. Devia, E. Restrepo-Parra, P.J. Arango, A.P. Tschiptschin, and J.M. Velez, Appl. Surf. Sci. **257**, 6181 (2011).

[42] D.M. Mattox, J. Vac. Sci. Technol. A Vacuum, Surfaces, Film. **7**, 1105 (1989).

[43] O. Karslioğlu, X. Song, H. Kuhlenbeck, and H.J. Freund, Top. Catal. **56**, 1389 (2013).

[44] J. Liu, Y. Lou, C. Zhang, S. Yin, H. Li, D. Sun, and X. Sun, RSC Adv. **7**, 43938 (2017).

[45] J.A. Sue and H.H. Troue, Surf. Coatings Technol. **33**, 169 (1987).

[46] S. Guruvenket and G. Mohan Rao, J. Vac. Sci. Technol. A Vacuum, Surfaces, Film. **20**, 678 (2002).

[47] C. Quaeyhaegens, G. Knuyt, J. D'Haen, and L.M. Stals, Thin Solid Films **258**, 170 (1995).

[48] D.R. McKenzie, Y. Yin, W.D. McFall, and N.H. Hoang, J. Phys. Condens. Matter **8**, 5883 (1996).

[49] A.C. Kozen, M.J. Sowa, L. Ju, N.C. Strandwitz, G. Zeng, T.F. Babuska, Z. Hsain, and B.A. Krick, J. Vac. Sci. Technol. A **37**, 061505 (2019).

[50] I. Krylov, Y. Qi, V. Korchnoy, K. Weinfeld, M. Eizenberg, and E. Yalon, J. Vac. Sci. Technol. A **38**, 032403 (2020).

[51] I. Krylov, X. Xu, Y. Qi, K. Weinfeld, V. Korchnoy, M. Eizenberg, and D. Ritter, J. Vac. Sci. Technol. A **37**, 060905 (2019).

[52] I. Krylov, E. Zoubenko, K. Weinfeld, Y. Kauffmann, X. Xu, D. Ritter, and M. Eizenberg, J. Vac. Sci. Technol. A **36**, 051505 (2018).

[53] Y.T. Yemane, M.J. Sowa, J. Zhang, L. Ju, E.W. Deguns, N.C. Strandwitz, F.B. Prinz, and J. Provine, Supercond. Sci. Technol. **30**, 095010 (2017).

[54] A. Nezu, H. Matsuzaka, and R. Yokoyama, Rigaku J. **30**, 4 (2014).

[55] C.H. Ma, J.H. Huang, and H. Chen, Thin Solid Films **418**, 73 (2002).

[56] X. Chen, Y. Xi, J. Meng, X. Pang, and H. Yang, J. Alloys Compd. **665**, 210 (2016).

[57] J.C. Goodrich, T.G. Farinha, L. Ju, A.J. Howzen, A. Kundu, O.N. Ogidi-Ekoko, J.J. Wierer, N. Tansu, and N.C. Strandwitz, J. Cryst. Growth **536**, (2020).

[58] J. Casamento, J. Wright, R. Chaudhuri, H. Xing, and D. Jena, Appl. Phys. Lett. **115**, 172101 (2019).